Hydrodynamic simulations of directed flow for light hadrons in Au+Au and isobar collisions at $\sqrt{s_{NN}}$ = 200 GeV*

Jing Jing (靖晶)[1]   Ze-Fang Jiang (江泽方)[1,2†]   C. B. Yang (杨纯斌)[2]   Ben-Wei Zhang (张本威)[2]

[1]Department of Physics and Electronic-Information Engineering, Hubei Engineering University, Xiaogan 432000, China
[2]Institute of Particle Physics and Key Laboratory of Quark and Lepton Physics (MOE), Central China Normal University, Wuhan 430079, China

Abstract: Using a (3+1)-D hydrodynamic model, CLVisc, we study the directed flow (v_1) of light hadrons produced in Au+Au, Ru+Ru, and Zr+Zr collisions at $\sqrt{s_{NN}}$ = 200 GeV. The evolution of tilted energy density, pressure gradient, and radial flow along the x-direction is systematically investigated. The counter-clockwise tilt of the initial fireball is shown to be a vital source of directed flow for final light hadrons. A good description of directed flow is provided for light hadrons in central and mid-central Au+Au and isobar collisions at the RHIC. Our numerical results show a clear system size dependence for light hadron v_1 across different collision systems. We further study the effect of nuclear structure on the directed flow and find that v_1 for light hadrons is insensitive to nuclei with quadrupole deformation.

Keywords: heavy ion collisions, quark-gluon plasma, directed flow, isobar Ru and Zr

I. INTRODUCTION

High energy nucleus-nucleus collisions performed at the Relativistic Heavy-Ion Collider (RHIC) and Large Hadron Collider (LHC) suggest that novel color-deconfined QCD matter (quark-gluon plasma, known as QGP) is created in the reaction region. The azimuthal asymmetric flows (collective flow) of the observed hadrons in various collision systems [1–3] are important phenomena in the study of the strongly interacting nature of QGP, such as directed flow v_1, elliptic flow v_2, and triangular flow v_3. Collective flows have been successfully described by relativistic hydrodynamic models [4–24], and the shear viscosity ratio (η_v/s) extracted from experimental data seems to be small [25, 26].

Directed flow (v_1) is one of earliest observables for investigating collectivity properties in heavy ion collisions [27–29]. It is defined by the first-order Fourier coefficient of the final-hadron azimuthal distribution and has been widely investigated at both the RHIC and LHC [30–37]. Many studies have suggested that directed flow is generated at an early stage in nuclear collisions, whose typical time scale is nearly $2R/\gamma$, where R and γ are the nuclear radius and Lorentz boost factor, respectively [6, 27, 38]. Such a time scale is even shorter than the production time of the elliptic flow v_2. Therefore, the directed flow v_1 could be a useful probe to investigate the medium distribution and nucleon flow at the initial stage of nucleus-nucleus collisions [4, 30, 38–43]. Various mechanisms may contribute to the directed flow of light hadrons. Model calculations suggest that v_1 may depend on the deformation of the initial fireball geometry, initial baryon density distribution, flow velocity field, equation of state of the QGP medium, external electromagnetic fields, and final hadronic rescatterings [40, 44–51], although their exact quantitative contributions are still unknown.

The recent isobar run of the collisions of both $^{96}_{44}$Ru and $^{96}_{40}$Zr[1) at $\sqrt{s_{NN}}$ = 200 GeV by the STAR Collaboration at the RHIC [52] had a special motivation: to search for the chiral magnetic effect (CME) [53–56]. However, the isobar blind analysis did not provide a predefined CME signal but surprisingly found that Ru+Ru collisions provided higher particle yields than Zr+Zr collisions, as well as a larger elliptic flow (v_2), albeit with a smaller tri-

1) We refer to $^{96}_{44}$Ru and $^{96}_{40}$Zr as Ru and Zr in the subsequent sections.

angular flow (v_3) [57, 58]. The differences in the experimental results at STAR indicate a difference in nuclear structure (geometry shape), whose observable effects are seemingly larger than those induced by the difference of the electric charge between Ru and Zr [52] and have been investigated from nuclear structure analyses in many studies [57, 59–65]. Therefore, it is of great interest to conduct a detailed comparison between Ru and Zr within a uniform QGP evolution framework and identify the main features of the nuclear structure (or system size) that contribute to the directed flow v_1 of identified final-state light hadrons.

In this study, we utilize a (3+1)-D viscous hydrodynamic model (CLVisc) with a tilted initial condition [66–68] to investigate the origin of the directed flow of light hadrons produced in Au+Au and isobar collisions at $\sqrt{s_{NN}} = 200$ GeV, with nuclear structure parameters for Ru and Zr from energy density functional theory (DFT) calculations [69–71]. The correlation between the fireball structure of the initial state and the directed flow coefficient of the final state light hadrons is presented. Our numerical results indicate that the tilted initial energy density profile for different nuclei (Au, Ru, and Zr) yields different nonzero average pressure gradients $-\langle \partial_x P \rangle$ at forward/backward space-time rapidity, which further induces a negative slope for the average flow velocity $\langle v_x \rangle$ with respect to the space-time rapidity η_s and eventually the same size and sign of v_1 *vs.* η, which is consistent with experimental data on Au+Au and isobar collisions at $\sqrt{s_{NN}} = 200$ GeV [52, 72, 73]. Our calculation shows a clear system size dependence for light hadron v_1 across different collision systems. In the end, we compare the directed flows (v_1) of three different nuclear structures with quadrupole deformation (β_2) for Ru and Zr nuclei.

The remainder of this article is organized as follows. In Sec. II, we present the rapidity-dependent energy density distributions in Au+Au and isobar collisions and their impacts on the pressure gradient and flow velocity with respect to time during hydrodynamic simulations. In Sec. III, we present the directed flow of light hadrons from our hydrodynamic calculation and study its dependence on the nuclear structure. We present a brief summary in Sec. IV.

II. MODEL FRAMEWORK

A. Parameterization of longitudinal profiles for energy density

To investigate the directed flow of light hadrons in Au+Au and isobar collisions, following our previous studies [74–77], we start with the initial energy density distributions of the nuclei Au, Ru, and Zr. Their impact on the pressure gradient and flow velocity with respect to

time is investigated using the (3+1)-D hydrodynamic model CLVisc.

Based on the Woods-Saxon (WS) distribution, the nucleus thickness function is defined as

$$T(x,y) = \int_{-\infty}^{\infty} dz \frac{n_0}{1 + \exp\left[\dfrac{r - R_0(1 + \beta_2 Y_2^0(\theta))}{d} \right]}, \quad (1)$$

where $r = \sqrt{x^2 + y^2 + z^2}$ is the radial position, x, y, z are the space coordinates, θ is the polar angle in their rest frame, d is the surface diffusiveness parameter, β_2 is the quadrupole deformation of the nucleus, $Y_2^0(\theta) = \frac{1}{4}\sqrt{\frac{5}{\pi}} \times (3\cos^2\theta - 1)$, and R_0 is the radius of the nucleus, which depends on the nucleus species. The values of the parameters used for Au, Ru, and Zr in the current study are listed in Table 1. At present, the nuclear density distributions of Ru and Zr are not accurately confirmed because there are a number of setups for parameters (R_0, d, and β_2) from different experiments and models. In this study, following the pioneering research [69–71] and STAR experiment [52], we first adopt the nuclei sets from recent calculations based on DFT [69–71, 78] to study light hadron directed flow. The other two sets are discussed later when we investigate the effect of nuclear structure on the directed flow v_1 of final light hadrons.

Considering the projectile and target nuclei propagating along the $\pm \hat{z}$ direction with the impact parameter $\boldsymbol{b}$, the corresponding thickness function can be written as

$$T_+(\boldsymbol{x}_T) = T(\boldsymbol{x}_T - \boldsymbol{b}/2), \quad T_-(\boldsymbol{x}_T) = T(\boldsymbol{x}_T + \boldsymbol{b}/2), \quad (2)$$

where $\boldsymbol{x}_T = (x, y)$ is the transverse plane coordinate. The density distributions of the participant nucleons are then given by

$$T_1(\boldsymbol{x}_T) = T_+(\boldsymbol{x}_T)\left\{ 1 - \left[1 - \frac{\sigma_{NN}T_-(\boldsymbol{x}_T)}{A} \right]^A \right\}, \quad (3)$$

$$T_2(\boldsymbol{x}_T) = T_-(\boldsymbol{x}_T)\left\{ 1 - \left[1 - \frac{\sigma_{NN}T_+(\boldsymbol{x}_T)}{A} \right]^A \right\}, \quad (4)$$

Table 1. Nuclear parameters used in the Woods-Saxon distribution for Au, Ru, and Zr [52, 79].

Nucleus	$n_0/(1/\text{fm}^3)$	R_0/fm	d/fm	β_2
$^{197}_{79}$Au	0.17	6.38	0.535	0.0
$^{96}_{44}$Ru	0.17	5.067	0.500	0.0
$^{96}_{40}$Zr	0.17	4.965	0.556	0.0

where A is the nucleus mass number, and $\sigma_{NN} = 42$ mb is the inelastic nucleon-nucleon scattering cross section at $\sqrt{s_{NN}} = 200$ GeV [79]. The centrality bins in different nuclear collisions are determined by the impact parameter $\boldsymbol{b}$ [79].

Because the right/left-moving wounded nucleons (as shown in Fig. 1) are expected to emit more particles at forward/backward rapidity, we assume this can be constructed by introducing a deformation mechanism into the weight function W_N [74], in which a tilted fireball is introduced to describe the observed charged particle directed flow in the RHIC and LHC energy region [74, 80]. In our earlier studies [74–76], a monotonic function ($T_1(x,y)+T_2(x,y)$) was modified to obtain the asymmetry between the forward and backward nuclei, as shown below.

$$W_N(x,y,\eta_s) = T_1(x,y) + T_2(x,y)$$
$$+ H_t[T_1(x,y) - T_2(x,y)]\tan\left(\frac{\eta_s}{\eta_t}\right), \quad (5)$$

where H_t reflects the strength of imbalance at the forward and backward rapidities, the function $\tan(\eta_s/\eta_t)$ produces the deformation of the initial energy density distribution along the longitudinal direction, and $\eta_t = 8.0$ is utilized for all collision systems [74]. In different centrality classes, the baryon stopping effect is different; hence, the contribution from the forward and backward nuclei are imbalanced. In our model, the parameter H_t reflects the strength of the baryon stopping effect and depends on the centrality. The value of H_t is extracted from the experimental data.

The total weight function $W(x,y,\eta_s)$ is defined as

$$W(x,y,\eta_s) = \frac{0.95 W_N(x,y,\eta_s) + 0.05 n_{BC}(x,y)}{[0.95 W_N(0,0,0) + 0.05 n_{BC}(0,0)]|_{b=0}}. \quad (6)$$

Here, the number of binary collisions $n_{BC}(x,y)$ is defined as [67, 79]

$$n_{BC}(x,y) = \sigma_{NN} T_+(x,y) T_-(x,y). \quad (7)$$

The initial energy density $\varepsilon(x,y,\eta_s)$ is given by [67]

$$\varepsilon(x,y,\eta_s) = K \cdot W(x,y,\eta_s) \cdot H(\eta_s), \quad (8)$$

where K is a normalization factor and determined by the multiplicity density distribution ($dN_{ch}/d\eta$) of soft particles. The function

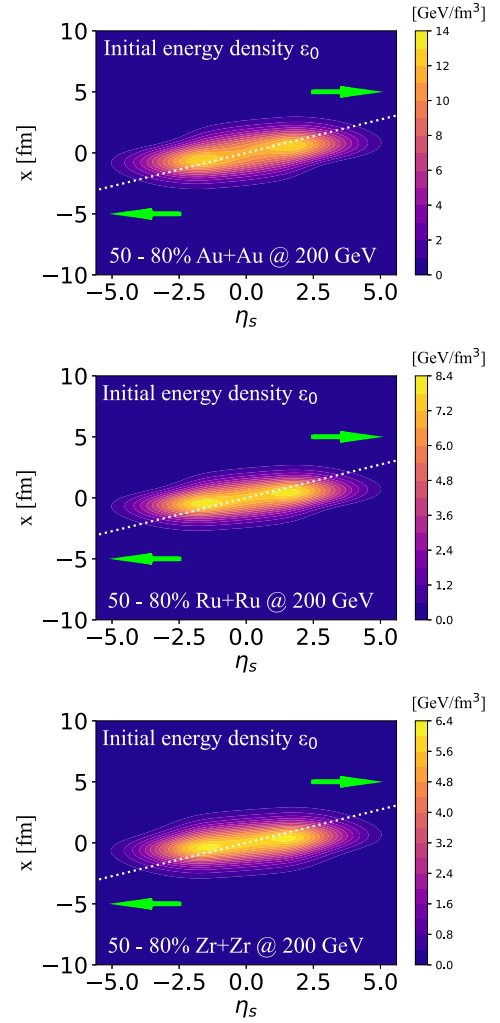$$H(\eta_s) = \exp\left[-\frac{(|\eta_s| - \eta_w)^2}{2\sigma_\eta^2}\theta(|\eta_s| - \eta_w)\right] \quad (9)$$

Fig. 1. (color online) Tilted initial energy density on the η_s-x plane at $\tau_0 = 0.6$ fm/c in 50%−80% Au+Au ($b = 11.4$ fm), Ru+Ru ($b = 9.3$ fm), and Zr+Zr ($b = 9.6$ fm) collisions at $\sqrt{s_{NN}} = 200$ GeV. The dotted line (white) shows the counterclockwise tilted initial condition with respect to the $x = 0$ axis in the η_s-x plane, and the arrow (green) indicates the motion at forward and backward rapidity.

is introduced to describe the plateau structure of the rapidity distribution of emitted hadrons at mid-rapidity, in which $\eta_w = 1.3$ determines the width of the central rapidity plateau, whereas $\sigma_\eta = 1.5$ determines the width (spread) of Gaussian decay from the plateau region [67].

In Table 2, we summarize the parameters of the initial conditions that are tuned to provide reasonable descriptions of the charged particle yields in the most central collisions [67], as shown in Figure 6. These include the overall normalization factor (K), initial time of hydrodynamic evolution (τ_0), impact parameters (b), and tilted parameters (H_t).

In present study, we set the initial fluid velocity in the transverse and space-time rapidity directions following the Bjorken approximation, that is, $v_x = v_y = 0$ and

Table 2. Parameters used in hydrodynamic simulations between different nuclei [67, 74, 75, 79].

Parameters	Au+Au	Ru+Ru	Zr+Zr
K/(GeV/fm^3)	35.5	23.0	23.0
τ_0/(fm/c)	0.6	0.6	0.6
b/fm	2.4	2.1	2.1
H_t	1.0	1.0	1.0

$v_z = z/t.$

B. Tilted energy density, eccentricity, and pressure gradient

Using the tilted initial condition above, we first present the energy density profile for different nuclei (Au, Ru, and Zr). In Fig. 1, we show the energy density profile for 50%–80% Au+Au, Ru+Ru, and Zr+Zr collisions at $\sqrt{s_{NN}} = 200$ GeV in the $\eta_s - x$ plane. Here, the model parameter $H_t = 4.5$ is taken for the Au+Au collisions (top panel), $H_t = 3.9$ is taken for the Ru+Ru collisions (middle panel), and $H_t = 3.1$ is taken for the Zr+Zr collisions (bottom panel). H_t is extracted from experimental data to describe the directed flow v_1 of charged particles and protons/anti-protons. From Fig. 1, the energy density distribution for different nuclei is not only shifted in the forward/backward rapidity direction but is also tilted counter-clockwise with respect to $x = 0$ [74, 80].

To quantify the asymmetry strength of the initial energy density for different nuclei at the initial state, we first present the first-order eccentricity coefficient ε_1 as a function of space-time rapidity in Fig. 2. The first-order eccentricity vector $\vec{\mathcal{E}}_1$ is defined as [15, 47]

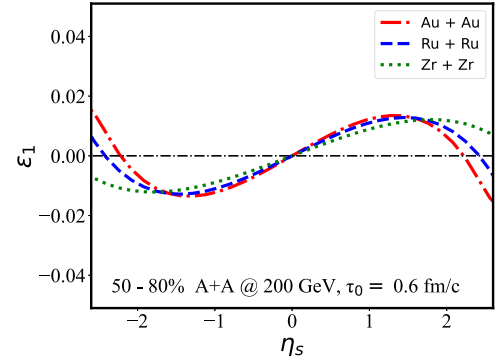$$\vec{\mathcal{E}}_1 \equiv \varepsilon_1(\eta_s)e^{i\Psi_1(\eta_s)} = -\frac{\int d^2\tilde{r}\tilde{r}^3 e^{i\tilde{\phi}}\varepsilon(r,\phi,\eta_s)}{\int d^2\tilde{r}\tilde{r}^3 \varepsilon(r,\phi,\eta_s)}, \quad (10)$$

where the angular distribution is calculated with respect to the energy density weighted center-of-mass point $(x_0(\eta_s), y_0(\eta_s))$ in every rapidity slice given by

$$x_0(\eta_s) = \frac{\int d^2 r x \varepsilon(r,\phi,\eta_s)}{\int d^2 r \varepsilon(r,\phi,\eta_s)}, \quad (11)$$

$$y_0(\eta_s) = \frac{\int d^2 r y \varepsilon(r,\phi,\eta_s)}{\int d^2 r \varepsilon(r,\phi,\eta_s)}, \quad (12)$$

where $\tilde{r}(x,y,\eta_s) = \sqrt{(x-x_0)^2 + (y-y_0)^2}$ is the transverse radius, and $\tilde{\phi}(x,y,\eta_s) = \arctan[(y-y_0)/(x-x_0)]$ is the azi-

Fig. 2. (color online) First-order eccentricity coefficient $\varepsilon_1(\eta_s)$ in 50%–80% nuclei-nuclei collisions at $\sqrt{s_{NN}} = 200$ GeV.

muthal angle. Note that ε_1 in Eq. (10) presents the first-order eccentricity coefficient, and Ψ_1 gives the corresponding participant plane angle. $\vec{\mathcal{E}}_1$ with respect to η_s quantifies the amount of tilt a fireball requires to produce light hadron v_1.

In Fig. 2, we present ε_1 as a function of space-time rapidity in 50%–80% Au+Au and isobar collisions at $\sqrt{s_{NN}} = 200$ GeV. ε_1 is an odd function of space-time rapidity η_s and is positive/negative in the $+/-\eta_s$ region. The slopes of ε_1 for three nuclei are positive at mid-rapidity but flip sign within $|\eta_s| > 1.5$. This further affects the evolution of the nuclear medium in the hydrodynamic simulation.

In addition to the initial energy density profile along the rapidity direction, we also present the initial pressure gradient $-\partial_x P$ in the transverse plane, which directly drives the radial flow of nuclear matter. In Fig. 3, the initial $-\partial_x P$ distribution in the *x-y* plane at a fixed forward rapidity $\eta_s = 1.2$ is presented for the nuclei Au, Ru, and Zr, where the parameter values of H_t and b are the same as those used for Fig. 1. One may clearly find the positive/negative value of the pressure gradient $-\partial_x P$ in the $+/-x$ direction leading to the outward expansion of the nuclear medium. From the top to bottom panels, we see that at $\eta_s = 1.2$, the center (zero pressure) regions of these distributions are shifted toward $+x$ owing to the counter-clockwise tilt of the initial energy density. Whether the average *x*-component of the final-state hadron momentum will be positive or negative at a given rapidity depends on the average magnitude of $-\partial_x P$ in the corresponding transverse plane and how it evolves with time. This is explored later in this paper.

C. Hydrodynamic evolution of QGP

We utilize the viscous hydrodynamic model CLVisc [66–68, 81, 82] to simulate the evolution of the QGP medium. The hydrodynamic equation satisfies [22, 83–86]
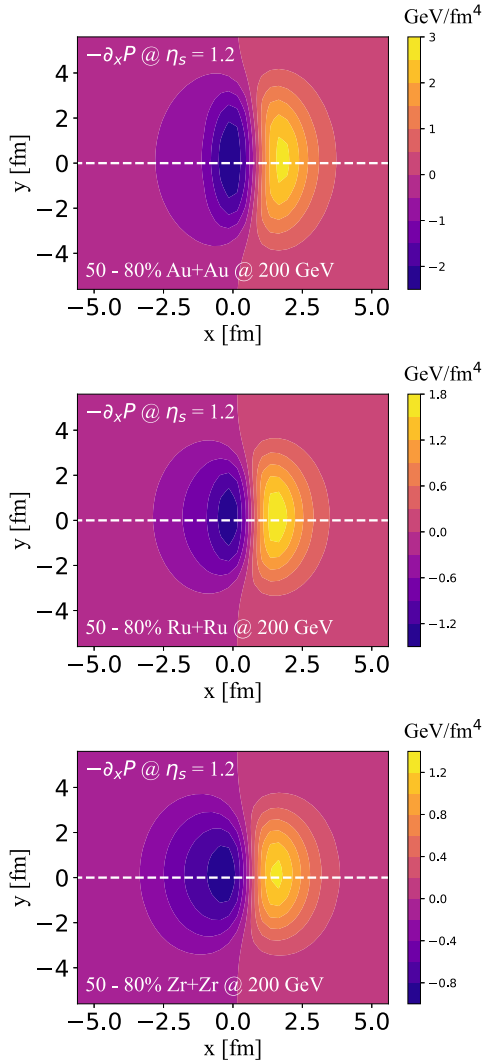
Fig. 3. (color online) Pressure gradient $-\partial_x P$ on the *x-y* plane at the initial proper time $\tau_0 = 0.6$ fm/*c* in 50%–80% Au+Au and isobar collisions.

$$\partial_\mu T^{\mu\nu} = 0, \tag{13}$$

where $T^{\mu\nu}$ is the energy-momentum tensor and takes the following form:

$$T^{\mu\nu} = \varepsilon u^\mu u^\nu - (P+\Pi)\Delta^{\mu\nu} + \pi^{\mu\nu}. \tag{14}$$

Here, ε is the energy density, u^μ is the fluid four-velocity field, P is the pressure, $\pi^{\mu\nu}$ is the shear stress tensor, and Π is the bulk pressure. The projection tensor is defined as $\Delta^{\mu\nu} = g^{\mu\nu} - u^\mu u^\nu$, and the metric tensor $g^{\mu\nu} = \mathrm{diag}(1,-1,-1,-1)$. In this study, we utilize the lattice QCD equation of state (EoS) from the Wuppertal-Budapest group (2014) [87], and the shear viscosity ratio is set as $\eta_v/s = 0.08$ (η_v for the shear viscosity) for all collision systems. Following recent studies [74, 75], the bulk viscosity and net ba-

ryon density are ignored at this moment but will be considered in our future studies [88, 89].

When the local temperature of nuclear matter drops below the freeze-out temperature (we set $T_{\mathrm{frz}} = 137$ MeV) [67], the Cooper-Frye mechanism [90] is used to calculate the spectra of hadrons on the freeze-out hypersurface. Contributions from resonance decay are taken into account according to our previous study [74, 75].

D. Evolution of average pressure gradient and flow velocity with respect to proper time

The hydrodynamic simulation presents how the imbalance of the initial energy density distribution is developed to the anisotropy of the final-state hadron momentum. In this subsection, we present how the fluid velocity $\langle v_x \rangle$ develops with respect to time at the opposite rapidity η_s. This will help us observe the development of the directed flow v_1 and how it depends on the tilted initial geometry of the energy density.

As presented in Fig. 3, the tilted initial energy density leads to asymmetry of the pressure gradient along the *x* direction. In Fig. 4, we present how the average pressure gradient $-\langle \partial_x P \rangle$ evolves with time at a given η_s (± 0.9 here) in 50%–80% Au+Au and isobar collisions at $\sqrt{s_{NN}} = 200$ GeV. We clearly observe that the evolution of $-\langle \partial_x P \rangle$ is significantly affected by the tilted initial en-
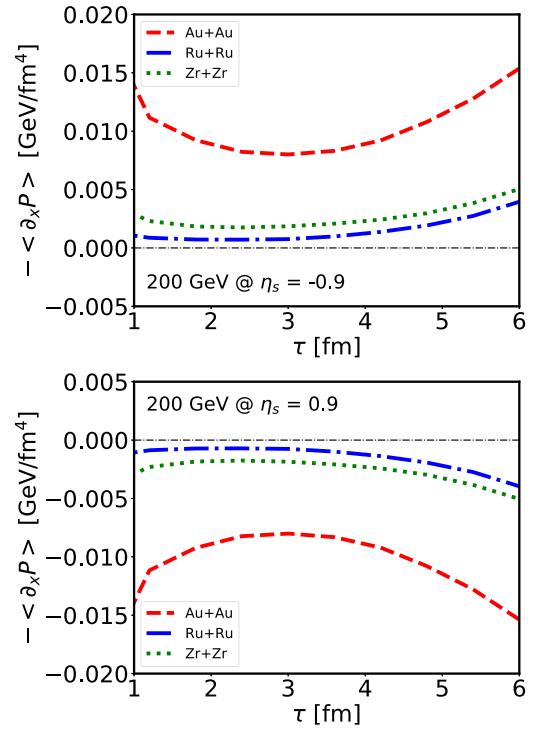

Fig. 4. (color online) Time evolution of the average pressure gradient in the *x* direction at $\eta_s = -0.9$ (upper panel) and $\eta_s = 0.9$ (lower panel) in 50%–80% Au+Au and isobar collisions at $\sqrt{s_{NN}} = 200$ GeV.

ergy density distribution. The evolution of the average pressure gradient $-\langle\partial_x P\rangle$ is anti-symmetric. We find that $-\langle\partial_x P\rangle$ remains positive with time at $\eta_s = -0.9$ and negative at $\eta_s = 0.9$, leading to a continuous force that accelerates QGP medium outward expansion toward the $+x$ direction at $\eta_s = -0.9$ and toward the $-x$ direction at $\eta_s = 0.9$. Little difference in the evolution of $-\langle\partial_x P\rangle$ is observed between the isobar Zr and Ru. Note that unlike the higher-order components of anisotropy, the first order eccentricity coefficient ε_1 and pressure gradient $-\langle\partial_x P\rangle$ are not necessarily positively correlated to each other.

Owing to the tilted deformation of nuclear matter, medium expansion contributes to an overall force toward the $+/-x$ direction at backward/forward rapidity. A direct outcome of such force is the asymmetric flow velocities in the corresponding direction. In Fig. 5, we present
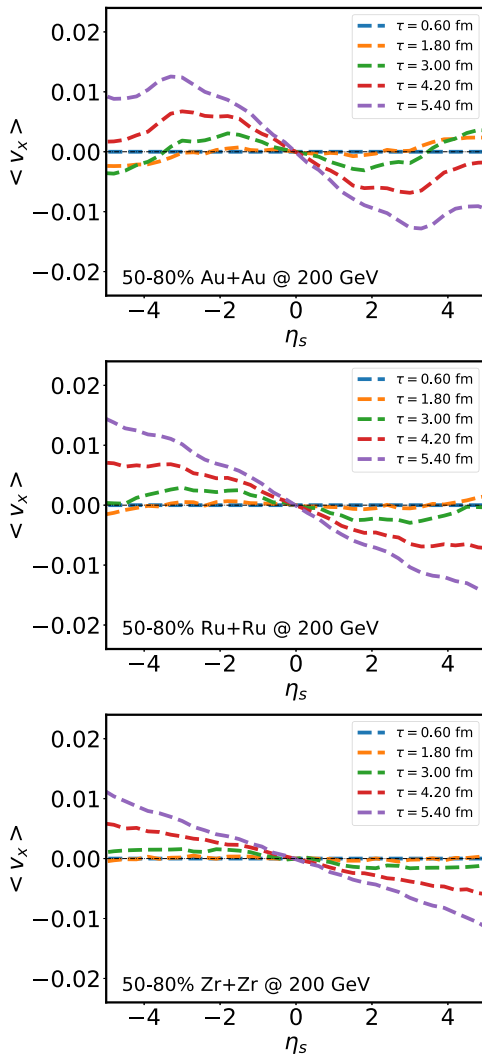

Fig. 5. (color online) Space-time rapidity dependence of the average flow velocity in the x direction at different evolution times in $50\%-80\%$ Au+Au and isobar collisions at $\sqrt{s_{NN}} = 200$ GeV.

how the average flow velocity $\langle v_x\rangle$ develops with time. The average flow velocity at a given proper time and space-time rapidity is defined as [16, 45]

$$\langle v_x(\eta_s)\rangle = \frac{\int \mathrm{d}^2 r v_x \gamma \varepsilon(r,\phi,\eta_s)}{\int \mathrm{d}^2 r \gamma \varepsilon(r,\phi,\eta_s)}, \qquad (15)$$

where $\gamma = 1/\sqrt{1 - v_x^2 - v_y^2 - v_{\eta_s}^2}$ is the Lorentz boost factor.

In Fig. 5, the average flow velocity $\langle v_x\rangle$ is positive/negative at backward/forward rapidity. The magnitude of $\langle v_x\rangle$ increases with time owing to the non-zero pressure gradient $-\langle\partial_x P\rangle$. We find that a larger $|-\langle\partial_x P\rangle|$ leads to a larger $\langle v_x\rangle$ at $|\eta_s|$ around the $|\eta_s| \approx 2$ regime than around the $|\eta_s| \approx 1$ regime. Here, the average flow velocity $\langle v_x\rangle$ will directly produce the directed flow of light hadrons.

III. NUMERICAL RESULTS

In this section, we present the numerical results for light hadrons yield and directed flow in Au+Au and isobar collisions at $\sqrt{s_{NN}} = 200$ GeV using the above tilted initial condition and the hydrodynamic model CLVisc. In particular, we investigate how the directed flow depends on the effect of the nuclear structure of the isobar Ru and Zr.

In Fig 6, we show the pseudorapidity distributions of the charged particles in Au+Au, Ru+Ru, and Zr+Zr collisions at $\sqrt{s_{NN}} = 200$ GeV. As discussed in Sec. IIA, the hydrodynamic model parameters summarized in Table 2 are adjusted to describe the charged light hadron distributions in the most central collisions. As shown in the figures, our calculation presents reasonable descriptions of PHOBOS data on the $\mathrm{d}N_{\mathrm{ch}}/\mathrm{d}\eta$ distributions for Au+Au collisions in several centralities at $\sqrt{s_{NN}} = 200$ GeV. In addition, note that the parameter H_t only affects the deformation of the medium geometry and has a weak impact on the $\mathrm{d}N_{\mathrm{ch}}/\mathrm{d}\eta$ distributions [75]. This provides a reliable baseline for further investigations on light hadron directed flow. We define centrality bins utilizing the impact parameter, and the contribution from the centrality fluctuation is not included in the current study. In the future, it will be necessary to use the multiplicity distribution with the given experimental data to characterize the centrality bins.

We then present the identified particle directed flow v_1 as a function of pseudorapidity. Following our previous research [74, 75], $v_1(\eta)$ is calculated via
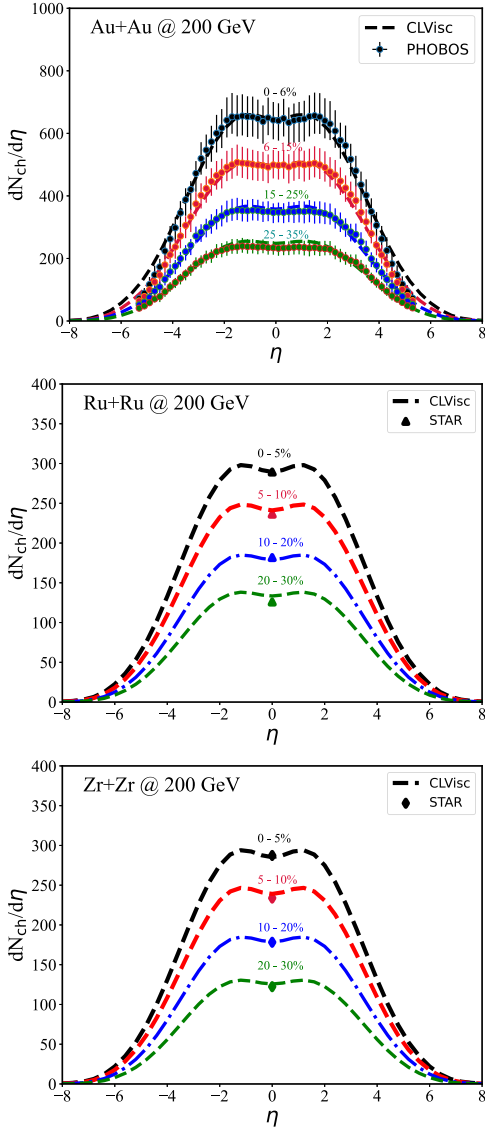
Fig. 6. (color online) Pseudorapidity distribution of charged light hadrons in Au+Au and isobar collisions at $\sqrt{s_{NN}} = 200$ GeV, compared between the CLVisc hydrodynamic calculation with three nuclei and PHOBOS and STAR data [52, 91].

$$v_1(\eta) = \langle \cos(\phi - \Psi_1) \rangle = \frac{\int \cos(\phi - \Psi_1) \frac{\mathrm{d}N}{\mathrm{d}\eta\mathrm{d}\phi} \mathrm{d}\phi}{\int \frac{\mathrm{d}N}{\mathrm{d}\eta\mathrm{d}\phi} \mathrm{d}\phi}, \qquad (16)$$

where Ψ_1 is the first-order event plane of the collision [45]. The directed flow v_1 is analyzed using soft hadrons within $0 < p_T < 3.0$ GeV in our current hydrodynamic model. Moreover, because the analysis usually uses $0.2 < p_T < 2.0$ GeV for charge particles, we will use this p_T range in future studies. Here, we use the optical Glauber model to construct the initial energy density distribution of nuclear matter, and the initial event-by-event

fluctuations are neglected [45, 74]. As a result, the event plane is the same as the spectator plane determined using deflected neutrons in realistic experimental measurements. The Monte Carlo Glauber model contributes the effect of event-by-event fluctuations, which enhances the directed flow at large forward and backward rapidity. A more consistent study will be conducted in future after event-by-event fluctuations are taken into account.

Using the above setups, we show light hadron v_1 in Au+Au collisions for different centrality classes at $\sqrt{s_{NN}} = 200$ GeV in Fig. 7; the upper panel for charged particles, and the lower for protons (p) and anti-protons ($\bar{p}$). Our calculations for charged particle v_1 within $-4.5 < \eta < 4.5$ are consistent with STAR data. As expected, the distribution of the identified particle v_1 is consistent with that of the average flow velocity v_x of nuclear matter.

For isobar collisions, as illustrated in Fig. 8, within our hydrodynamic framework, we are able to describe the directed flow v_1 of protons ($p^{\pm}$) at either Ru+Ru or Zr+Zr by adjusting the H_t parameter. The difference in the v_1 value between the two nuclei is less than 0.001 within $|y| < 1.5$. If the value of H_t is decreased, the slope of v_1 vs. y decreases near the mid-rapidity region and further deviates from the experimental data. This implies the
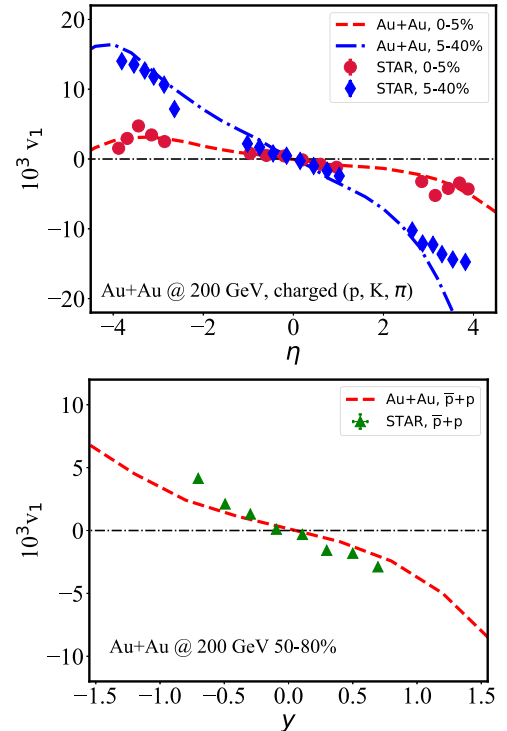

Fig. 7. (color online) Pseudorapidity and rapidity dependence of the directed flow of identified hadrons in 0 −5%, 5%−40% (upper panel), and 50%−80% (lower panel) Au+Au collisions at $\sqrt{s_{NN}} = 200$ GeV, compared between the CLVisc hydrodynamic calculation with STAR data [72, 73].
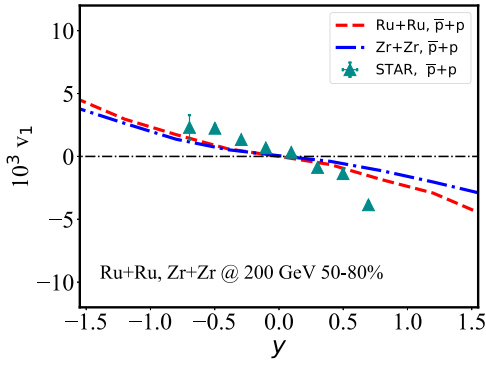
Fig. 8.　(color online) Rapidity dependence of the directed flow coefficient in 50%–80% Ru+Ru and Zr+Zr collisions at $\sqrt{s_{NN}} = 200$ GeV, compared between the CLVisc hydrodynamic calculation with the Case-1 nuclear structure and STAR data [73].

Table 3.　Nuclear structure parameters for Ru and Zr from Ref. [52].

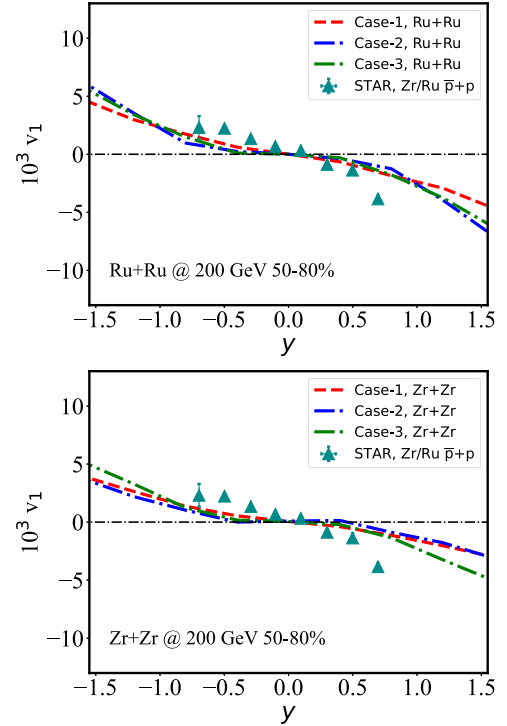| Parameter	Case-1		Case-2		Case-3	
	Ru+Ru	Zr+Zr	Ru+Ru	Zr+Zr	Ru+Ru	Zr+Zr
R/fm	5.067	4.965	5.085	5.02	5.085	5.02
d/fm	0.500	0.556	0.46	0.46	0.46	0.46
β_2	0.0	0.0	0.158	0.08	0.053	0.217

Fig. 9.　(color online) Rapidity dependence of the directed flow coefficient in 50%–80% Ru+Ru collisions (upper panel) and Zr+Zr collisions (lower panel) at $\sqrt{s_{NN}} = 200$ GeV, compared between the CLVisc hydrodynamic calculation with three nuclear structure setups and STAR data [73].

importance of the tilted initial energy density distribution in understanding the rapidity dependence of light hadron v_1 observed in experiments. Based on Figs. 7 and 8, we find that with a different H_t for isobar and Au+Au collisions at the same centrality bins, a clear system size dependence is observed for directed flow. Smaller nuclei have a smaller H_t, which leads to a smaller directed flow at mid-rapidity.

Thus far, we have focused on the discussion of spherical nuclei (from DFT) in which the quadrupole deformity parameter $\beta_2 = 0$ (as listed in Table 1). As noted in Refs. [57, 59–65], elliptic flow in the most central collisions is sensitive to nuclear deformation because deformed nuclei colliding at the impact parameter $b = 0$ can induce a large eccentricity on the collision orientation. To study the effect of nuclear deformation on light hadron v_1 within our hydrodynamic framework, the extended WS parameters of nuclei listed in Table 3 are utilized. The two sets (Case-2 and Case-3) have the same R and a parameters and different deformations, which are constrained by $e + A$ scattering experiments and calculations based on a finite-range droplet macroscopic model [92, 93] and the folded-Yukawa single-particle microscopic model [94]. Because of the additional protons in Ru, the charge radius of Ru is larger than that of Zr. Other parameters during QGP evolution are the same as those of spherical nuclei (Case-1).

Figure 9 shows the proton v_1 in Ru+Ru/Zr+Zr collisions at $\sqrt{s_{NN}} = 200$ GeV with various combinations of Ru and Zr deformities. The comparison between the three nuclear structures shows that β_2 deformations may not be essential to change the v_1 slope and magnitude at central pseudorapidity ($|y| < 0.5$). We see that the slope of v_1 changes insignificantly due to finite β_2 between Case-2 and Case-3 for both Ru+Ru and Zr+Zr collisions. The impact of the different parameters R, d, and β_2 on proton v_1 implies that the nuclear structure with quadrupole de-

formation only slightly affects the directed flow of final state particles. We note here that v_1 between Ru and Zr at a large rapidity may be sensitive to the shape of the nuclei. Furthermore, many low energy experiments have shown that Zr has a large octupole deformation corresponding to a large value of β_3. Theoretical studies have found that the average of the first-order eccentricity coefficient ε_1 is proportional to the average of β_3^2, and the octupole deformation should affect the v_1 of soft hadrons [59, 95]. The effect of octupole deformation will be investigated in an upcoming study.

Note that because we use the optical Glauber model (smooth initial condition), our calculation is restricted to the rapidity-odd component of light hadron v_1. The rapidity-even component v_1^{even}, including its non-trivial p_T dependence [96–98], is beyond the scope of this study and

will be investigated in the future.

IV. SUMMARY

In this paper, we present a systematic investigation of how the initial medium profile of nuclei evolves to light hadron directed flow in heavy ion collisions. Three different nucleus-nucleus collisions (Au+Au, Ru+Ru, and Zr+Zr) are compared for the tilted initial energy density distribution, and their subsequent space-time evolutions are simulated utilizing the hydrodynamic model CLVisc.

Using our (3+1)-D hydrodynamic model CLVisc, we calculate the directed flow v_1 for light hadrons as a function of (pseudo-)rapidity and centrality for Au+Au and isobar collisions at $\sqrt{s_{NN}}$ = 200 GeV. Our model can give a good description of light hadron v_1 in central and peripheral Au+Au and isobar collisions measured by the STAR Collaboration. Our results show that light hadron v_1 has a strong system size dependence, that is, v_1 is larger for small systems, owing to a weaker nuclear stopping effect. The system size dependence is also observed from the centrality dependence: v_1 becomes large when moving from central to peripheral collisions, which is clearly observed in Au+Au collisions and can be tested by future experiments. We further find that the Au+Au and isobar semi-central collisions generate an imbalance between a forward/backward moving nucleus, induce a counter-clockwise tilt of the initial medium profile in the x-η_s plane, and generate a non-zero average pressure gradient $-\langle \partial_x P \rangle$ with respect to time at backward/forward rapidity. A comparison to RHIC-STAR data indicates that the tilted initial energy density profile (or fireball geometry) is an essential factor in generating the observed light hadron v_1 in Au+Au and isobar collisions at

$\sqrt{s_{NN}}$ = 200 GeV. We finally find that the effect of nuclear structure with quadrupole deformation insignificantly affects the light hadron directed flow at mid-rapidity.

Our study provides a step toward understanding the origin of light hadron directed flow in Au+Au and isobar collisions. However, in addition to the effect of tilted initial energy density, other sources also contribute to the size and sign of directed flow. See the following examples: (1) The extremely strong electromagnetic field produced in non-central nucleus-nucleus collisions results in directional drift of charged quarks (u, d, s) and influences the charged particle v_1 [99–101]. Although this effect is suggested to be smaller than the effect of the initial tilted geometry, it is important to understand the splitting of v_1 for identified light hadrons in isobar collisions [99]. (2) The fluid velocity field could provide an additional contribution to light hadron directed flow [48]. In particular, it could affect the initial baryon density distribution and thus nuclear matter properties [45]. (3) Light hadron v_1 can also be affected by the nuclear stopping effect and hadronic cascade after QGP evolution, especially at lower collision energies [47, 48, 51]. (4) The light hadron elliptic flow v_2 and triangular flow v_3 could set more constraints on the nuclear structure; however, we do not discuss this here because we limit ourselves to a smooth initial condition without the contribution of event-by-event fluctuations. These should be investigated in our future studies for a more exact understanding of directed flow.

References

[1] S. S. Adler *et al*., Phys. Rev. Lett. **91**, 182301 (2003)
[2] K Aamodt *et al*., Phys. Rev. Lett. **105**, 252302 (2010)
[3] S. Chatrchyan *et al*., Phys. Rev. C **87**(1), 014902 (2013)
[4] Jean-Yves Ollitrault, Phys. Rev. D **46**, 229-245 (1992)
[5] Dirk H. Rischke, S. Bernard, and J. A. Maruhn, Nucl. Phys. A **595**, 346-382 (1995)
[6] H. Sorge, Phys. Rev. Lett. **78**, 2309-2312 (1997)
[7] S.A. Bass, M. Gyulassy, H. Stoecker *et al*., J. Phys. G **25**, R1-R57 (1999)
[8] C. E. Aguiar, Y. Hama, T. Kodama *et al*., Nucl. Phys. A **698**, 639-642 (2002)
[9] E. Shuryak, Prog. Part. Nucl. Phys. **53**, 273-303 (2004)
[10] M. Gyulassy and L. McLerran, Nucl. Phys. A **750**, 30-63 (2005)
[11] W. Broniowski, P. Bozek, and M. Rybczynski, Phys. Rev. C **76**, 054905 (2007)
[12] R. P. G. Andrade, F. Grassi, Y. Hama *et al*., Phys. Rev. Lett. **101**, 112301 (2008)
[13] T. Hirano and Y. Nara, Phys. Rev. C **79**, 064904 (2009)
[14] B. Schenke, Sangyong Jeon, and C. Gale, Phys. Rev. Lett. **106**, 042301 (2011)
[15] Zhi Qiu and Ulrich W. Heinz, Phys. Rev. C **84**, 024911 (2011)
[16] U. Heinz and R. Snellings, Ann. Rev. Nucl. Part. Sci. **63**, 123-151 (2013)
[17] P. Huovinen, Int. J. Mod. Phys. E **22**, 1330029 (2013)
[18] C. Gale, Sangyong Jeon, and B. Schenke, Int. J. Mod. Phys. A **28**, 1340011 (2013)
[19] P. Bozek and W. Broniowski, Phys. Rev. C **88**(1), 014903 (2013)
[20] Guang-You Qin, and B. Müller, Phys. Rev. C **89**(4), 044902 (2014)
[21] K. Dusling, Wei Li, and B. Schenke, Int. J. Mod. Phys. E **25**(01), 1630002 (2016)
[22] P. Romatschke and U. Romatschke. *Relativistic Fluid Dynamics In and Out of Equilibrium*. Cambridge Monographs on Mathematical Physics, (Cambridge University Press, 5 2019)
[23] R. D. Weller and P. Romatschke, Phys. Lett. B **774**, 351-356 (2017)

[24] Wenbin Zhao, Che Ming Ko, Yu-Xin Liu *et al*., Phys. Rev. Lett. **125**(7), 072301 (2020)

[25] Huichao Song, Steffen A. Bass, Ulrich Heinz *et al*., Phys. Rev. Lett., **106**, 192301 (2011) [Erratum: Phys. Rev. Lett. **109**, 139904 (2012)]

[26] Jonah E. Bernhard, J. Scott Moreland, and Steffen A. Bass, Nature Phys. **15**(11), 1113-1117 (2019)

[27] M. Gyulassy, K. A. Frankel, and Horst Stoecker, Phys. Lett. B **110**, 185-188 (1982)

[28] H. A. Gustafsson *et al*., Phys. Rev. Lett. **52**, 1590-1593 (1984)

[29] Michael Annan Lisa, Ulrich W. Heinz, and Urs Achim Wiedemann, Phys. Lett. B **489**, 287-292 (2000)

[30] S. Voloshin and Y. Zhang, Z. Phys. C **70**, 665-672 (1996)

[31] A. Bilandzic, R. Snellings, and S. Voloshin, Phys. Rev. C **83**, 044913 (2011)

[32] J. Adams *et al*., Phys. Rev. C **72**, 014904 (2005)

[33] L. Adamczyk *et al*., Phys. Rev. Lett. **112**(16), 162301 (2014)

[34] L. Adamczyk *et al*., Phys. Rev. Lett. **120**(6), 062301 (2018)

[35] J. Adam *et al*., Phys. Rev. Lett. **123**(16), 162301 (2019)

[36] S. Acharya *et al*., Phys. Rev. Lett. **125**(2), 022301 (2020)

[37] Jaroslav Adam *et al*., Phys. Rev. C **101**(2), 024905 (2020)

[38] S. Singha, P. Shanmuganathan, and D. Keane, Adv. High Energy Phys. **2016**, 2836989 (2016)

[39] Y. Nara, H. Niemi, A. Ohnishi, and H. Stöcker, Phys. Rev. C **94**(3), 034906 (2016)

[40] S. Chatterjee and P. Bozek, Phys. Rev. Lett. **120**(19), 192301 (2018)

[41] Chao Zhang, Jiamin Chen, Xiaofeng Luo *et al*., Phys. Rev. C **97**(6), 064913 (2018)

[42] Chong-Qiang Guo, Chun-Jian Zhang, and Jun Xu, Eur. Phys. J. A **53**(12), 233 (2017)

[43] Tribhuban Parida and Sandeep Chatterjee, *Splitting of elliptic flow in a tilted fireball*, arXiv: 2204.02345

[44] A. Adil and M. Gyulassy, Phys. Rev. C **72**, 034907 (2005)

[45] P. Bozek and I. Wyskiel, Phys. Rev. C **81**, 054902 (2010)

[46] Baoyi Chen, Maoxin Hu, Huanyu Zhang *et al*., Phys. Lett. B **802**, 135271 (2020)

[47] Chun Shen and S. Alzhrani, Phys. Rev. C **102**(1), 014909 (2020)

[48] Sangwook Ryu, Vahidin Jupic, and Chun Shen, Phys. Rev. C **104**(5), 054908 (2021)

[49] S. Chatterjee and P. Bozek, Phys. Lett. B **798**, 134955 (2019)

[50] A. Beraudo, A. De Pace, M. Monteno *et al*., JHEP **05**, 279 (2021)

[51] Piotr Bozek, *Splitting of proton-antiproton directed flow in relativistic heavy-ion collisions*, arXiv: 2207.04927

[52] Mohamed Abdallah *et al*., Phys. Rev. C **105**(1), 014901 (2022)

[53] Kenji Fukushima, Dmitri E. Kharzeev, and Harmen J. Warringa, Phys. Rev. D **78**, 074033 (2008)

[54] V. Skokov, A. Yu. Illarionov, and V. Toneev, Int. J. Mod. Phys. A **24**, 5925-5932 (2009)

[55] Wei-Tian Deng, Xu-Guang Huang, Guo-Liang Ma *et al*., Phys. Rev. C **94**, 041901 (2016)

[56] Xin-Li Zhao, Guo-Liang Ma, and Yu-Gang Ma, Phys. Rev. C **99**(3), 034903 (2019)

[57] Govert Nijs and Wilke van der Schee, *Inferring nuclear structure from heavy isobar collisions using Trajectum*, arXiv: 2112.13771

[58] Chunjian Zhang, *Somadutta Bhatta, and Jiangyong Jia. Ratios of collective flow observables in high-energy isobar collisions are insensitive to final state interactions*, arXiv: 2206.01943

[59] Chunjian Zhang and Jiangyong Jia, Phys. Rev. Lett. **128**(2), 022301 (2022)

[60] Jiangyong Jia and Chun-Jian Zhang, *Scaling approach to nuclear structure in high-energy heavy-ion collisions*, arXiv: 2111.15559

[61] Hao-jie Xu, Wenbin Zhao, Hanlin Li et al., *Probing nuclear structure with mean transverse momentum in relativistic isobar collisions*, arXiv: 2111.14812

[62] Fei Li, Yu-Gang Ma, Song Zhang *et al*., *Impact of nuclear structure on the CME background in $^{96}_{44}$Ru + $^{96}_{44}$Ru and $^{96}_{40}$Zr + $^{96}_{40}$Zr collisions at $\sqrt{s_{NN}}$ = 7.7 ~ 200 GeV from a multiphase transport model*, arXiv: 2201.10994

[63] Xin-Li Zhao and Guo-Liang Ma, Phys. Rev. C **106**(3), 034909 (2022)

[64] Yu-Gang Ma and Song Zhang, *Influence of nuclear structure in relativistic heavy-ion collisions*, arXiv: 2206.08218

[65] Jiangyong Jia, Giuliano Giacalone, and Chunjian Zhang, *Precision tests of the nonlinear mode coupling of anisotropic flow via high-energy collisions of isobars*, arXiv: 2206.07184

[66] Long-Gang Pang, H. Petersen, Qun Wang *et al*., Phys. Rev. Lett. **117**(19), 192301 (2016)

[67] Long-Gang Pang, H. Petersen, and Xin-Nian Wang, Phys. Rev. C **97**(6), 064918 (2018)

[68] Xiang-Yu Wu, Long-Gang Pang, Guang-You Qin *et al*., Phys. Rev. C **98**(2), 024913 (2018)

[69] Hao-Jie Xu, Xiaobao Wang, Hanlin Li *et al*., Phys. Rev. Lett. **121**(2), 022301 (2018)

[70] Hanlin Li, Hao-jie Xu, Jie Zhao *et al*., Phys. Rev. C **98**(5), 054907 (2018)

[71] Hao-jie Xu, Hanlin Li, Xiaobao Wang *et al*., Phys. Lett. B **819**, 136453 (2021)

[72] B.I. Abelev *et al*., Phys. Rev. Lett. **101**, 252301 (2008)

[73] A. I. Sheikh (for the STAR Collaboration), *Splitting of directed flow for identified light hadrons (π, K, p) and strange baryons (Ξ, Ω) in Au+Au and isobar collisions at STAR*, 29th Conference on Ultra-telativistic Nucleus-Nucleus Collisions – Quark Matter 2022

[74] Ze-Fang Jiang, C. B. Yang, and Qi Peng, Phys. Rev. C **104**(6), 064903 (2021)

[75] Ze-Fang Jiang, Shanshan Cao, Xiang-Yu Wu *et al*., Phys. Rev. C **105**(3), 034901 (2022)

[76] Ze-Fang Jiang, Shanshan Cao, Wen-Jing Xing *et al*., Phys. Rev. C **105**(5), 054907 (2022)

[77] Xiaowen Li, Ze-Fang Jiang, Shanshan Cao *et al*., *Evolution of global polarization in relativistic heavy-ion collisions within a perturbative approach*, arXiv: 2205.02409

[78] Wei-Tian Deng, Xu-Guang Huang, Guo-Liang Ma *et al*., Phys. Rev. C **97**(4), 044901 (2018)

[79] C. Loizides, J. Kamin, and D. d'Enterria, Phys. Rev. C, **97**(5), 054910 (2018) [Erratum: Phys. Rev. C **99**, 019901 (2019)]

[80] Piotr Bozek, Phys. Rev. C **85**, 034901 (2012)

[81] Wei Chen, Shanshan Cao, Tan Luo *et al*., Phys. Lett. B **777**, 86-90 (2018)

[82] Yayun He, Long-Gang Pang, and Xin-Nian Wang, Phys.

Rev. Lett. **122**(25), 252302 (2019)

[83] Ze Fang Jiang, Duan She, C.B. Yang *et al*., Chin. Phys. C **44**(8), 084107 (2020)

[84] Ze-Fang Jiang, C.B. Yang, Chi Ding *et al*., Chin. Phys. C **42**(12), 123103 (2018)

[85] G.S. Denicol, H. Niemi, E. Molnar *et al*., Phys. Rev. D **85**, 114047 (2012)

[86] P. Romatschke, Int. J. Mod. Phys. E **19**, 1-53 (2010)

[87] S. Borsanyi, Z. Fodor, C. Hoelbling *et al*., Phys. Lett. B **730**, 99-104 (2014)

[88] Wenbin Zhao, Weiyao Ke, Wei Chen *et al*., Phys. Rev. Lett. **128**(2), 022302 (2022)

[89] Xiang-Yu Wu, Guang-You Qin, Long-Gang Pang *et al*., Phys. Rev. C **105**(3), 034909 (2022)

[90] F. Cooper and G. Frye, Phys. Rev. D **10**, 186 (1974)

[91] B. Alver *et al*., Phys. Rev. C **83**, 024913 (2011)

[92] S. Raman, C. W. G. Nestor, Jr, and P. Tikkanen, Atom. Data Nucl. Data Tabl. **78**, 1-128 (2001)

[93] B. Pritychenko, M. Birch, B. Singh *et al*., Atom. Data Nucl. Data Tabl., **107**, 1–139 (2016) [Erratum: Atom.Data Nucl.Data Tabl. **114**, 371–374 (2017)]

[94] P. Moller, J. R. Nix, W. D. Myers *et al*., Data Nucl. Data Tabl. **59**, 185-381 (1995)

[95] Jiangyong Jia, Phys. Rev. C **105**(1), 014905 (2022)

[96] Derek Teaney and Li Yan, Phys. Rev. C **83**, 064904 (2011)

[97] Matthew Luzum and Jean-Yves Ollitrault, Phys. Rev. Lett. **106**, 102301 (2011)

[98] Charles Gale, Sangyong Jeon, Bjìrn Schenke *et al*., Phys. Rev. Lett. **110**(1), 012302 (2013)

[99] G. Inghirami, M. Mace, Y. Hirono *et al*., Eur. Phys. J. C **80**(3), 293 (2020)

[100] U. GUrsoy, D. E. Kharzeev, and K. Rajagopal, Phys. Rev. C **89**(5), 054905 (2014)

[101] U. Gürsoy, D. E. Kharzeev, E. Marcus *et al*., Phys. Rev. C **98**(5), 055201 (2018)